RSC Advances

PAPER

View Article Online
View Journal | View Issue

Cite this: *RSC Adv.*, 2026, **16**, 25515

Effect of divalent cation substitution (M = Mn, Ni, Mg, Cu) on the structural, magnetic and electrical properties of MFe_2O_4 spinel ferrites

Ibtihel Soudani, *[a] Nazir Mustapha[b] and Mokhtar Hjiri*[b]

In This study, a systematic investigation of the influence of the nature of the divalent cation (M^{2+} = Ni, Mg, Cu, Mn) on the multifunctional properties of spinel ferrites MFe_2O_4 synthesized by solid-state reaction is presented. X-ray diffraction (XRD) analyses validate the formation of single-phase cubic phases (space group $Fd\bar{3}m$). Despite significant disparities between the ionic radii of the M^{2+} cations (0.69 to 0.80 Å), the lattice retains its integrity, highlighting the high structural robustness of these materials in the face of cationic substitution. The precise determination of the oxidation states and the distribution of metal ions between the tetrahedral and octahedral sites of our prepared samples is carried out by X-ray photoelectron spectroscopy (XPS), while Raman spectroscopy corroborates these results by identifying the five vibrational modes characteristic of the spinel structure. Magnetic characterizations reveals that the ferrites $MnFe_2O_4$ and $NiFe_2O_4$ exhibit the highest saturation magnetizations (M_s), whereas $MgFe_2O_4$ shows a reduced magnetization due to the non-magnetic nature of the Mg^{2+} ion. The compound $CuFe_2O_4$ exhibits intermediate values, influenced by Jahn–Teller distortions and the mixed valence states of copper. The coercivity (H_c) varies depending on the cation, classifying some samples as soft magnetic materials, optimal for low-energy-loss applications. Furthermore, high-frequency analyses demonstrate that substitution engineering allows these ferrites to be optimized for microwave devices. Finally, electrical measurements performed between 400 and 700 K reveal remarkable performance for thermal sensing. Combined with an excellent stability factor, these properties authenticate the reliability of these materials for high-temperature sensor applications.

Received 29th March 2026
Accepted 11th May 2026

DOI: 10.1039/d6ra02603f

rsc.li/rsc-advances

1 Introduction

Spinel ferrites, with the general formula MFe_2O_4 (M^{2+} = Mn, Ni, Mg, Cu), have been extensively investigated for decades due to their unique combination of magnetic, electrical, and structural properties. This multifunctionality makes them highly attractive for a wide range of technological applications.[1–5] These materials crystallize in a face-centered cubic structure, where oxygen anions form a close-packed lattice and cations are distributed between tetrahedral (A) and octahedral (B) sites. This flexible cationic distribution plays a crucial role in determining the fundamental properties of spinel ferrites, including saturation magnetization, coercivity, and electrical resistivity.[6,7] In particular, partial cationic inversion in nickel ferrite nanostructures has been reported to enhance magnetic hardening, coercive field, and magnetic anisotropy due to changes in the cation occupancy between tetrahedral (A) and octahedral (B) sites and the resulting modification of superexchange interactions.[8]

Spinel ferrites are semiconducting materials widely used in diverse fields such as gas sensing, heterogeneous catalysis, energy storage, wastewater treatment, magnetic resonance imaging (MRI), and high-frequency electromagnetic wave absorption.[9,10] Beyond their conventional applications in electronics and microwave devices, these materials have recently gained increasing attention for biomedical applications, particularly in magnetic hyperthermia and cancer therapy.[11] In such applications, their performance can be significantly enhanced through precise control of chemical composition and microstructure.[12]

Recent studies have emphasized the importance of compositional engineering in tuning the structural, magnetic, electrical, and optical properties of spinel ferrites. For instance, Zn–Ni[13,14] and Mn–Zn[15] ferrites exhibit enhanced magneto-functional and optical properties under optimized processing conditions, while $MgFe_2O_4$- and $CoFe_2O_4$-based systems have demonstrated improved dielectric performance and microwave absorption efficiency.[16] In addition, hybridization strategies, including graphene incorporation and multivalent ion substitution, have been shown to significantly affect AC conductivity, dielectric relaxation, and thermal stability.[17,18] These findings

[a]*Laboratory of Multifunctional Materials and Applications (LaMMA), LR16ES18, Faculty of Sciences of Sfax, University of Sfax, BP 1171, 3000 Sfax, Tunisia. E-mail: ebtihel.soudani@gmail.com*

[b]*Department of Physics, College of Sciences, Imam Mohammad Ibn Saud Islamic University (IMSIU), Riyadh 11623, Saudi Arabia. E-mail: mbhjiri@imamu.edu.sa*

highlight that compositional flexibility and microstructural control are key factors in the rational design of next-generation multifunctional ferrite materials.

Despite the large number of studies on individual ferrite compositions such as $MnFe_2O_4$, $NiFe_2O_4$, $MgFe_2O_4$, and $CuFe_2O_4$, comparative investigations under strictly identical synthesis conditions remain limited. Such an approach is essential to isolate the intrinsic effect of the divalent cation on structural order, magnetic response, and electrical behavior, while eliminating variations arising from synthesis routes or particle size effects. Moreover, establishing clear correlations between cation nature, crystallographic structure, and functional properties is critical for optimizing ferrites for targeted applications, including sensors, inductors, microwave devices, and multifunctional systems.[19–21]

In this work, we present a systematic comparative study of $MnFe_2O_4$, $NiFe_2O_4$, $MgFe_2O_4$, and $CuFe_2O_4$ ferrites synthesized under identical experimental conditions. Structural (XRD), vibrational (Raman), and surface (XPS) analyses are combined with magnetic and electrical measurements to elucidate the influence of the divalent cation on lattice parameters, cation distribution, electronic states, magnetic behavior, and dielectric properties. This approach allows a direct structure–property correlation, providing deeper insight into the fundamental mechanisms governing spinel ferrites and offering guidance for the design of advanced materials for electronic, magnetic, and energy-related applications.

2 Experimental procedure

2.1 Preparation of samples

Spinel ferrite powders with nominal compositions MFe_2O_4 (M^{2+} = Mn, Ni, Mg, Cu) are synthesized by the conventional solid-state reaction method, as illustrated in Fig. 1. High-purity metal oxides are utilized as precursors (99.9%, Sigma-Aldrich): the phases are obtained by combining MnO, CuO, MgO and NiO with Fe_2O_3, respectively. Each oxide mixture is scrupulously weighted to obtain the desired stoichiometry. Then, it is mechanically ground in an agate mortar for a total of 6 hours. This thorough homogenization process not only reduced particle size but also significantly increased the reactivity of the precursor powders. Afterwards, the homogenized powders are well grinding, then it is compacted into cylindrical pellets in order of 8 mm in diameter and 1 mm in thickness using a uniaxial hydraulic press. To eliminate any residual organic material, the substances produced are subjected to a calcination cycle for 24 h at 1000 °C to enhance grain crystallization. At last, the pellets are annealed in ambient air at 1200 °C for 9 hours. This last step is the sintering which is important step to ensure a high sample densification and promoting the formation of a well-defined spinel phase.

2.2 Characterization techniques

The crystalline structure and vibrational properties of the samples are analyzed by X-ray diffraction (XRD) on a Panalytical system using Cu-Kα radiation (0.02° step size) and by Raman spectroscopy using a SENTERRA Spectrometer (Bruker) with green laser excitation of 540 nm. The surface chemical composition is examined by X-ray photoelectron spectroscopy (XPS) on a Thermo Scientific Kα instrument. Magnetic characterizations are performed using an extraction magnetometer, M(H) cycles up to 5 T at room temperature. Finally, the electrical behavior is probed by impedance spectroscopy (Solartron 1260) over a wide thermal range from 400 K to 700 K. For these measurements, platinum electrodes are applied to the sintered disks to obtain stable ohmic contacts, the tests being carried

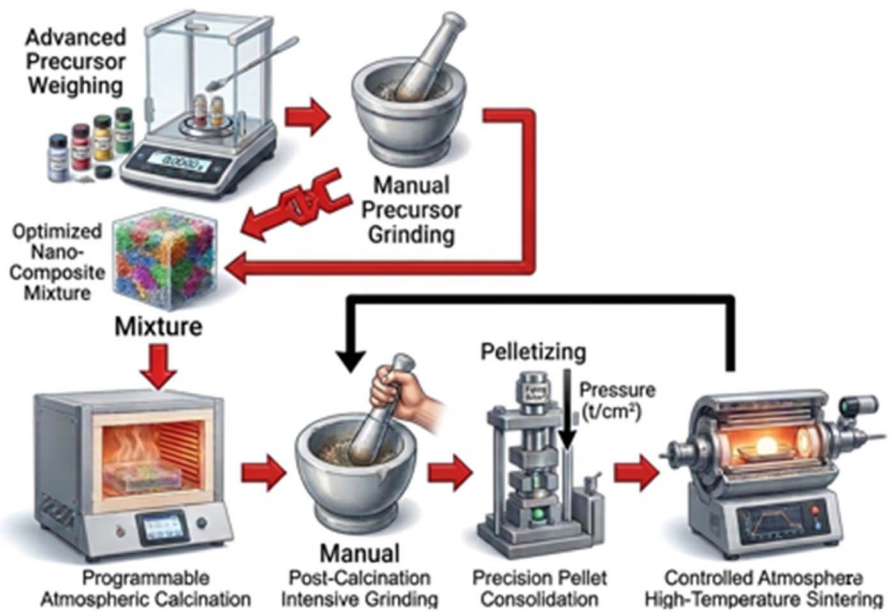

Fig. 1 Elaboration method of MFe_2O_4 (M^{2+} = Mn, Cu, Ni, Mg) compound using the solid-state route.

out at thermal equilibrium under ambient air to validate the reproducibility of the results.

3 Results and discussion

3.1 Structural analysis

To evaluate the influence of the divalent cation M^{2+} (M = Mn, Ni, Mg, Cu) on the crystal structure of spinel ferrites, X-ray diffraction (XRD) data collected at room temperature were analyzed using the Rietveld refinement method with FullProf software.[5] The XRD patterns (Fig. 2a–d) confirm the formation of a single-phase cubic spinel structure with space group $Fd\bar{3}m$, with no detectable secondary phases, indicating high crystalline purity.

The refined profiles show good agreement between the calculated and experimental data, as reflected by the reliability factors and goodness-of-fit ($\chi^2 \approx 1$). The structural parameters obtained from the refinement are summarized in Table 1. The crystal structures, projected along the (011) plane and visualized using VESTA software, are shown in the insets of Fig. 2.

The evolution of lattice parameters reveals a systematic variation correlated with the ionic radius of the M^{2+} cations (Mn^{2+}: 0.83 Å, Cu^{2+}: 0.73 Å, Mg^{2+}: 0.72 Å, Ni^{2+}: 0.69 Å,.[22] A monotonic increase in lattice parameter and unit cell volume is observed with increasing ionic radius, in agreement with Vegard's law.[23] This behavior reflects the accommodation of larger cations within the spinel lattice, leading to lattice expansion and local structural relaxation. Similar trends have been reported in the literature, where cation substitution influences crystallinity and cation distribution between tetrahedral (A) and octahedral (B) sites.[24–27]

Furthermore, the (311) diffraction peak, which is the most intense reflection, exhibits a systematic shift toward lower 2θ values (Fig. 3), indicating an increase in interplanar spacing according to Bragg's law. This shift further confirms the lattice expansion induced by larger M^{2+} cations.

It is important to note that spinel ferrites are rarely perfectly stoichiometric systems. The presence of intrinsic defects such as oxygen vacancies and cationic disorder can induce local lattice distortions and influence structural properties. These defects may also lead to mixed valence states (*e.g.*, Fe^{3+}/Fe^{2+}), which play a significant role in charge transport mechanisms *via* polaron hopping.[28]

To ensure a rigorous evaluation of the microstructural parameters, the crystallite size and lattice strain were decoupled using the Williamson–Hall (W–H) equation. Unlike the simplified Scherrer equation,[29] which attributes peak broadening solely to size effects, the W–H approach accounts for the inherent micro-strain ε resulting from lattice distortions and defects. The W–H plots and the extracted parameters are presented in Fig. 4.

The average crystallite size which presented in Fig. 4 is determined by Williamson–Hall (W–H) equation:[30]

$$\beta \cos \theta = 4\varepsilon \sin \theta + \frac{k\lambda}{D_{WH}} \quad (1)$$

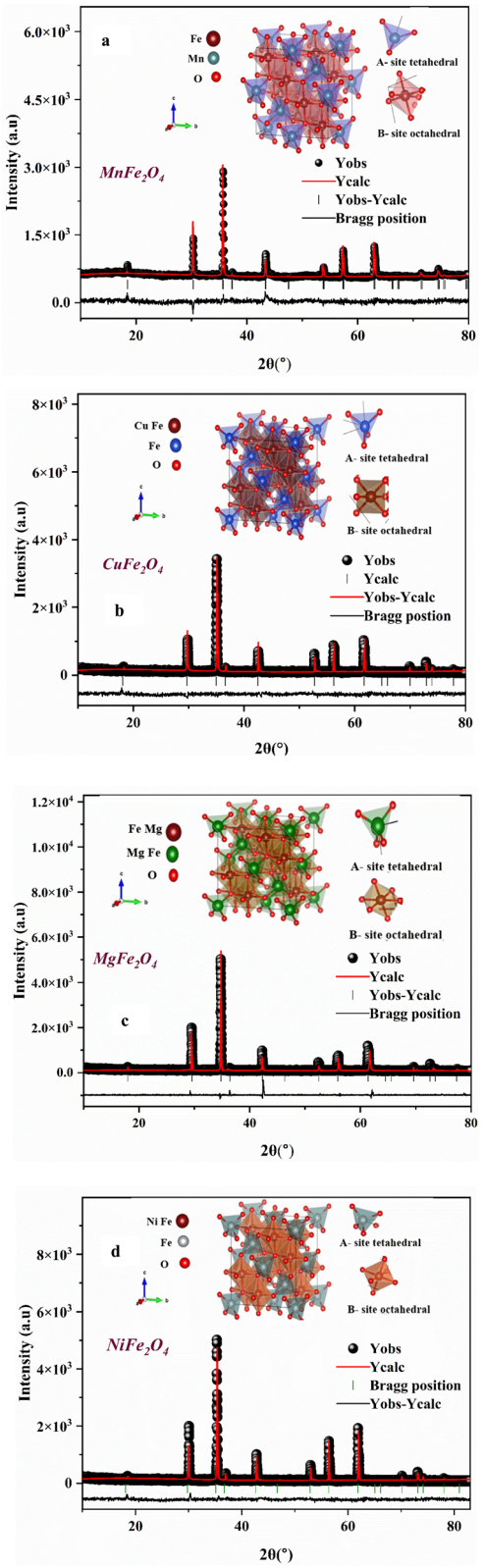

Fig. 2 X-ray diffraction patterns of MFe_2O_4 (M^{2+} = Ni, Mg, Cu, Mn) spinel ferrites with Rietveld analysis. Mn (a), Cu (b), Mg (c), and Ni (d).

In which β is a full width at half maximum (FWHM) which was determined by peak fitting using a pseudo-Voigt function after background subtraction. The fitting procedure was

Table 1 Structural parameters of MFe_2O_4 (M^{2+} = Ni, Mg, Cu, Mn) spinel ferrites derived from Rietveld refinement

Formula	$MnFe_2O_4$	$CuFe_2O_4$	$MgFe_2O_4$	$NiFe_2O_4$
Crystallin system	Cubic	Cubic	Cubic	Cubic
Space group	$Fd\bar{3}m$	$Fd\bar{3}m$	$Fd\bar{3}m$	$Fd\bar{3}m$
Lattice parameter (Å)				
$a = b = c$	8.41	8.37	8.39	8.36
$\alpha = \beta = \gamma$ (°)	90	90	90	90
V (Å^3)	594.82	586.37	590.59	584
Reliability factors (%)				
R_p (%)/R_{wp} (%)/R_{exp} (%)	6.61/8.68/6.30	6.24/8.43/3.81	6.94/9.75/7.11	6.01/8.28/4.20
Goodness of fit χ^2	1.64	1.48	1.54	1.18

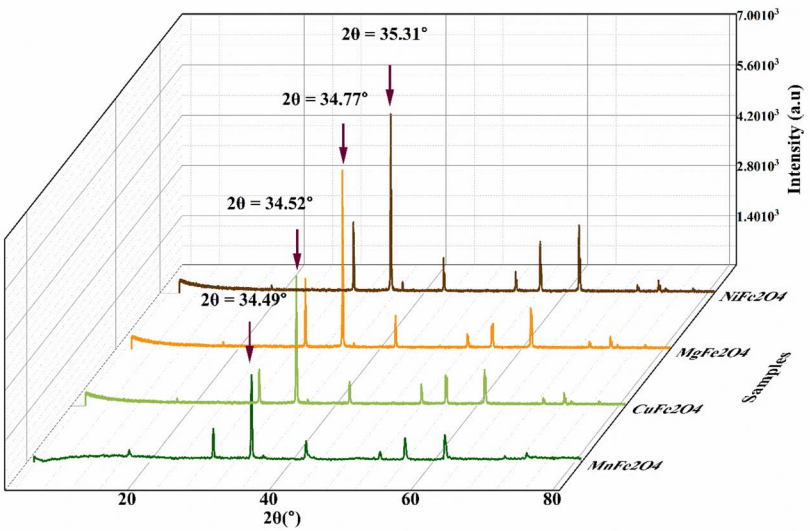

Fig. 3 The position of the diffraction peak (311) for MFe_2O_4 (M^{2+} = Ni, Mg, Cu, Mn).

performed using FullProf software, allowing accurate extraction of peak position and width. θ is the diffraction angle and 15 416 A is the Cu-Kα wavelength of the radiation.

The variation in crystallite size can be attributed to the development of microstrain and structural defects arising from the mismatch between the ionic radii of M^{2+} cations and Fe^{3+} ions. This mismatch induces lattice distortion and local disorder, which tend to hinder grain growth. The associated strain energy favors nucleation over crystal growth, resulting in relatively small crystallite sizes.

Although the nature of the M^{2+} cation influences the crystallite size, the relatively similar values observed for all samples suggest that crystal growth is mainly governed by synthesis conditions, particularly the high-temperature treatment. The slightly larger crystallite size observed for $CuFe_2O_4$ can be attributed to the Jahn–Teller effect associated with Cu^{2+} ions, which induces local distortion and may facilitate cation diffusion, thereby promoting grain growth.[31]

Overall, these results highlight the strong influence of cation substitution and defect chemistry on the structural properties of spinel ferrites. The interplay between ionic size, lattice distortion, and defect formation provides an effective way to tune the structural and functional properties of these materials.[32]

3.2 Vibrational analysis

The analysis of the crystal structure and lattice dynamics is further investigated using confocal Raman spectroscopy, a technique known for its sensitivity to atomic vibrations and its ability to probe cationic disorder and phase transitions in ferrites.[33] Raman spectra, recorded at room temperature between 120 and 850 cm^{-1} under 540 nm laser excitation (Fig. 5), validate the chemical purity and phase formation of the spinel ferrite samples. According to factor group analysis for a spinel structure belonging to the $Fd\bar{3}m$ space group, the theory predicts five Raman active modes:[34]

$$\xi = A_{1g} + E_g + 3\ T_{2g} \quad (2)$$

resulting from the movements of oxygen ions and cations occupying sites A and B.[35] More specifically, mode A_{1g} is attributed to the symmetric stretching of the metal–oxygen bond in tetrahedral sites, while mode E_g reflects the symmetric bending of oxygen with respect to the cations in octahedral

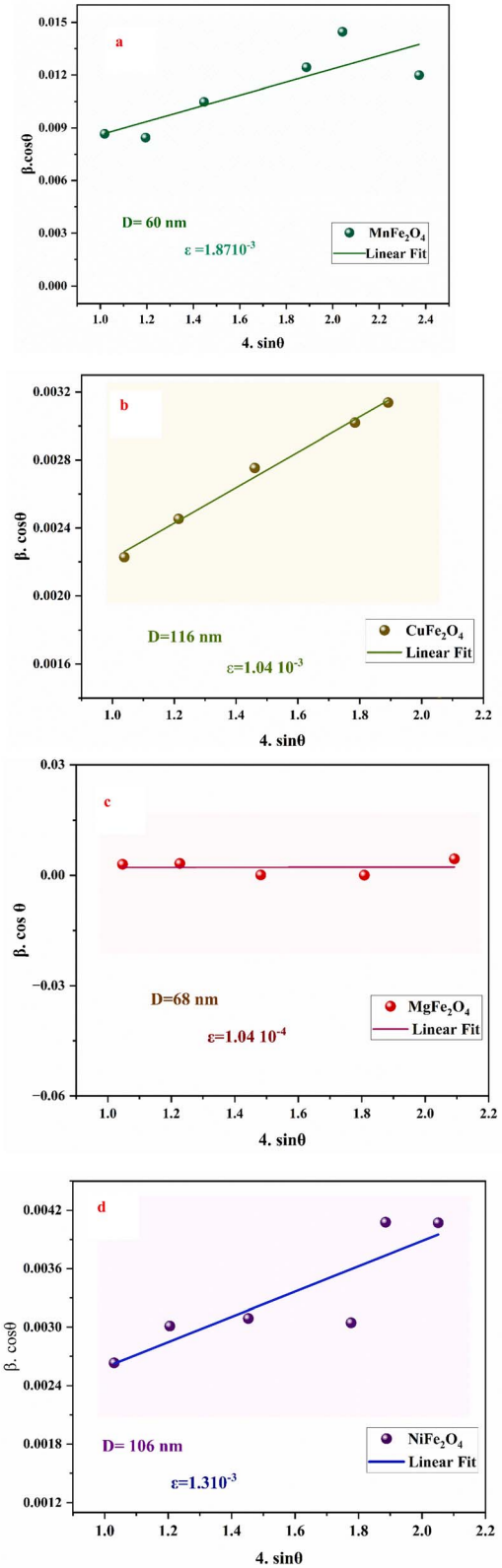

Fig. 4 The Williamson–Hall (W–H) plots of spinel ferrites: Mn (a), Cu (b), Mg (c), and Ni (d).

sites. Finally, modes $T_{2g}(3)$ and $T_{2g}(2)$ arise from symmetric and asymmetric bending movements within the structure, respectively. This vibrational signature complements the XRD study by validating the structural stability and the phase purity of the spinel system under investigation. The $T_{2g}(1)$ mode is attributed to the global translational motion of the tetrahedral units.[36] The Raman bands observed for the different samples MFe_2O_4 (M = Mn, Cu, Mg, Ni) are in perfect agreement with the theoretical vibrational modes expected for the $Fd\bar{3}m$ space group. This structural correspondence, combined with the absence of spurious peaks in the spectra, corroborates the X-ray diffraction (XRD) analyses and thus confirms the single-phase nature of all the compounds studied. The purity of these spinel phases guarantees that the observed resistivity variations and thermal sensitivities result intrinsically from the lattice dynamics and the cationic distribution specific to each ferrite.[37]

To extract the frequency and full width at half maximum (FWHM) parameters, the spectra are fitted using Lorentzian profiles. Then, it is tabulated in Table 2. In spinel ferrites, frequencies above 600 cm^{-1} are associated with oxygen vibrations in tetrahedral sites (AO_4), while lower modes correspond to the octahedral sublattice.[38] The appearance of "shoulder bands" likely results from a breaking of the momentum conservation rule, linked to the electrical and vibrational behavior of MFe_2O_4 ferrites (M = Mn, Cu, Mg, Ni) is intrinsically linked to the redistribution of cations between tetrahedral (A) and octahedral (B) sites, a phenomenon governed by the ionic radius and the field stabilization energy of the ligands.[39]

The vibrational behavior of spinel ferrites is strongly influenced by the distribution of cations between A and B sites, which depends on factors such as ionic radius and crystal field stabilization energy.[39] For instance, Mn^{2+} ions (0.83 Å) tend to occupy tetrahedral sites, leading to a predominantly normal spinel structure, whereas Ni^{2+} ions (0.69 Å) preferentially occupy octahedral sites, resulting in an inverse spinel configuration. This redistribution is quantified by the inversion degree (i), which significantly affects bond lengths, lattice dynamics, and charge transport mechanisms.[40]

Additional structural distortions, such as the Jahn–Teller effect associated with Cu^{2+} ions, or the partially inverse character of $MgFe_2O_4$, further modify the local symmetry and vibrational behavior. These effects are reflected in the Raman spectra by shifts in peak positions and changes in band widths.

In particular, the A_{1g} mode exhibits a systematic shift toward higher frequencies from $MnFe_2O_4$ to $NiFe_2O_4$, which can be attributed to the decrease in ionic radius and the corresponding increase in metal–oxygen bond strength.[41] Moreover, the broadening of Raman bands, especially in $MnFe_2O_4$ and $CuFe_2O_4$, suggests enhanced cationic disorder and microstructural effects such as reduced crystallite size or lattice strain.[42]

Overall, these results demonstrate that Raman spectroscopy is a powerful tool for probing cation distribution, inversion degree, and defect-induced structural distortions in spinel ferrites, providing complementary insights to XRD analysis.[43]

3.3 X-ray photoelectron spectroscopy (XPS) analysis

X-ray photoelectron spectroscopy (XPS) was employed to investigate the surface chemical composition and oxidation states of MFe_2O_4 (M = Mn, Ni, Mg, Cu) spinel ferrites. The survey spectra

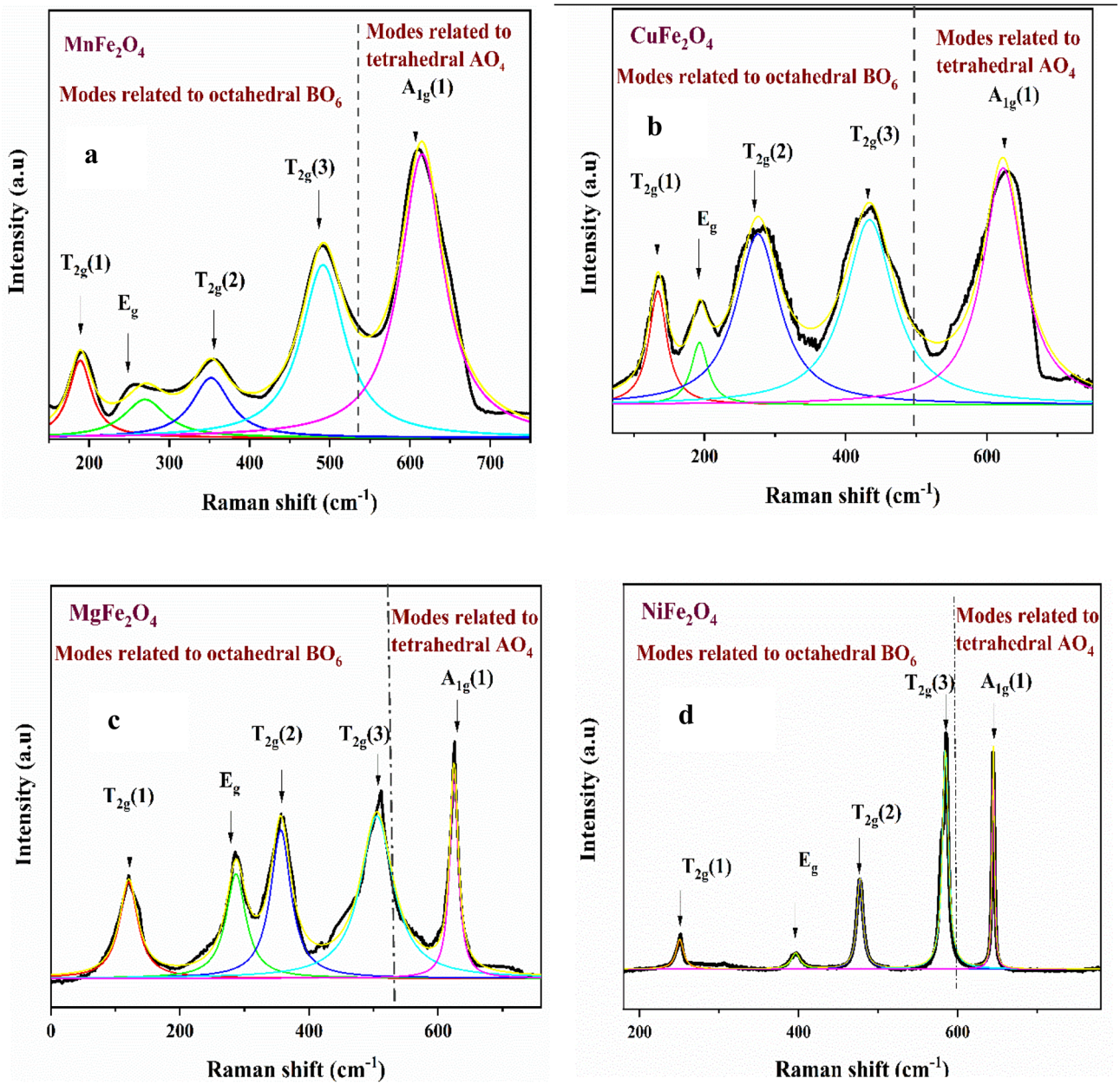

Fig. 5 Raman spectra of (a) $MnFe_2O_4$, (b) $CuFe_2O_4$, (c) $MgFe_2O_4$ and (d) $NiFe_2O_4$ spinel ferrites.

Table 2 Raman band position of the tetrahedral and octahedral sites of MFe_2O_4 (M = Mn, Cu, Mg, Ni) spinel ferrites samples

	Raman band									
	A_{1g}		$T_{2g}(3)$		$T_{2g}(2)$		E_g		$T_{2g}(1)$	
Samples	Position (cm^{-1})	FWHM	Position (cm^{-1})	FWHM	Position (cm^{-1})	FWHM	Position (cm^{-1})	FWHM	Position (cm^{-1})	FWHM
$MnFe_2O_4$	615	66	492	66	352	57	270	64	189	35
$CuFe_2O_4$	623	69	434	84	276	75	193	29	134	31
$MgFe_2O_4$	625	16	505	61	356	38	287	37	121	35
$NiFe_2O_4$	645	3	585	8	477	9	396	14	251	11

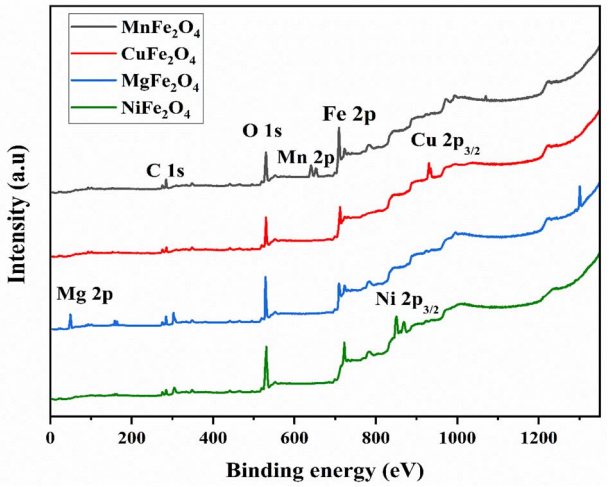

Fig. 6 X-ray photoelectron spectroscopy (XPS) survey spectra of MFe_2O_4 (M^{2+} = Ni, Mg, Cu, Mn) spinels ferrites.

recorded over the binding energy range of 0–1350 eV (Fig. 6) confirm the presence of Fe, O, and the corresponding divalent cations (Mn, Ni, Mg, and Cu). A C 1s peak is also observed, originating from adventitious carbon contamination on the sample surface.[44] No additional impurity peaks are detected, indicating the high chemical purity of the samples.

The XPS spectra were fitted after Shirley background subtraction using Gaussian–Lorentzian (pseudo-Voigt) functions. The fitting procedure was performed using Origin, allowing accurate determination of peak positions, intensities, and satellite features.

The high-resolution Fe 2p spectra (Fig. 7) exhibit a characteristic doublet with binding energies located at approximately 710–711 eV (Fe $2p_{3/2}$) and 723–725 eV (Fe $2p_{1/2}$). In addition, satellite features are clearly observed at about 7.8 eV above the main peaks (as indicated in Fig. 7), which are characteristic of Fe^{3+} ions and arise from shake-up processes.[45] These features confirm that iron predominantly exists in the Fe^{3+} oxidation state in all samples.

Slight variations in peak positions and relative intensities are observed among $MnFe_2O_4$, $NiFe_2O_4$, $MgFe_2O_4$, and $CuFe_2O_4$, reflecting differences in local chemical environments and cation distribution within the spinel lattice.

The Mn 2p spectrum of $MnFe_2O_4$ shows two main peaks located at approximately 641 eV (Mn $2p_{3/2}$) and 653 eV (Mn $2p_{1/2}$), consistent with the presence of Mn^{2+} ions.[46] For $NiFe_2O_4$, the Ni 2p spectrum exhibits peaks at ~855–856 eV and ~872–873 eV, confirming the Ni^{2+} oxidation state.[47] The Mg 2p peak in $MgFe_2O_4$ appears around 48–49 eV, indicating the presence of Mg^{2+} ions. In the case of $CuFe_2O_4$, the Cu 2p spectrum shows a characteristic doublet at ~934 eV and ~954 eV, along with asymmetry features associated with Cu^{2+} ions and Jahn–Teller distortion effects.[48–50]

The O 1s spectra (Fig. 7) can be deconvoluted into two main components. The dominant peak at ~529.5–530.0 eV corresponds to lattice oxygen (O^{2-}) associated with metal–oxygen bonds (M–O–Fe) in the spinel structure.[51] The second component, located in the range 531–532 eV, is attributed to surface oxygen species and/or oxygen vacancies. The variation in the relative intensity of this component among the samples indicates differences in defect concentration, which may significantly influence electrical conductivity and magnetic properties.[52]

Overall, the XPS results confirm the formation of single-phase spinel ferrites composed of divalent cations (Mn^{2+}, Ni^{2+}, Mg^{2+}, Cu^{2+}) and trivalent Fe^{3+} ions. The observed variations in binding energies, cation distribution, and oxygen-related defects highlight the strong influence of the M^{2+} cation on the surface electronic structure, which plays a key role in determining the functional properties of these materials.

3.4 Magnetic properties and hysteresis loop analysis

The magnetic properties of MFe_2O_4 (M = Mn, Cu, Mg, Ni) spinel ferrites were investigated at room temperature using hysteresis (M–H) measurements (Fig. 8). All samples exhibit typical ferrimagnetic behavior, characterized by a rapid increase in magnetization at low magnetic fields followed by a tendency toward saturation at higher fields. The main magnetic parameters, including saturation magnetization (M_s), remanent magnetization (M_r), and coercive field (H_c), are summarized in Table 3. These parameters strongly depend on the nature of the divalent cation M^{2+}, its magnetic moment, ionic radius, and its distribution between tetrahedral (A) and octahedral (B) sites (Fig. 9).

$MnFe_2O_4$ exhibits the highest saturation magnetization, which can be attributed to the high magnetic moment of Mn^{2+} ions and their contribution to A–B superexchange interactions.[53] In contrast, $MgFe_2O_4$ shows the lowest M_s due to the non-magnetic nature of Mg^{2+} ions, which weakens the magnetic coupling between sublattices.[54] $NiFe_2O_4$ presents intermediate behavior, consistent with its inverse spinel structure where Ni^{2+} ions preferentially occupy octahedral sites.[55] $CuFe_2O_4$ is distinguished by a relatively higher coercive field, which is mainly attributed to the Jahn–Teller effect of Cu^{2+} ions. This effect induces local lattice distortions, enhances magneto-crystalline anisotropy, and increases resistance to magnetization reversal.[56,57] Overall, the relatively low H_c values indicate that the studied ferrites behave as soft magnetic materials, although $CuFe_2O_4$ shows a tendency toward harder magnetic behavior.[58]

The magneto-crystalline anisotropy constant (K_1) was estimated using the Stoner–Wohlfarth relation:[59]

$$K_1 = \frac{H_c \times M_s}{0.98} \quad (3)$$

The obtained values indicate that $CuFe_2O_4$ exhibits the highest anisotropy, whereas $MgFe_2O_4$ shows the lowest value. $NiFe_2O_4$ and $MnFe_2O_4$ present intermediate values, reflecting the influence of electronic configuration and spin–orbit coupling. In addition to intrinsic factors, microstructural features such as crystallite size and internal strain also contribute to the effective anisotropy.

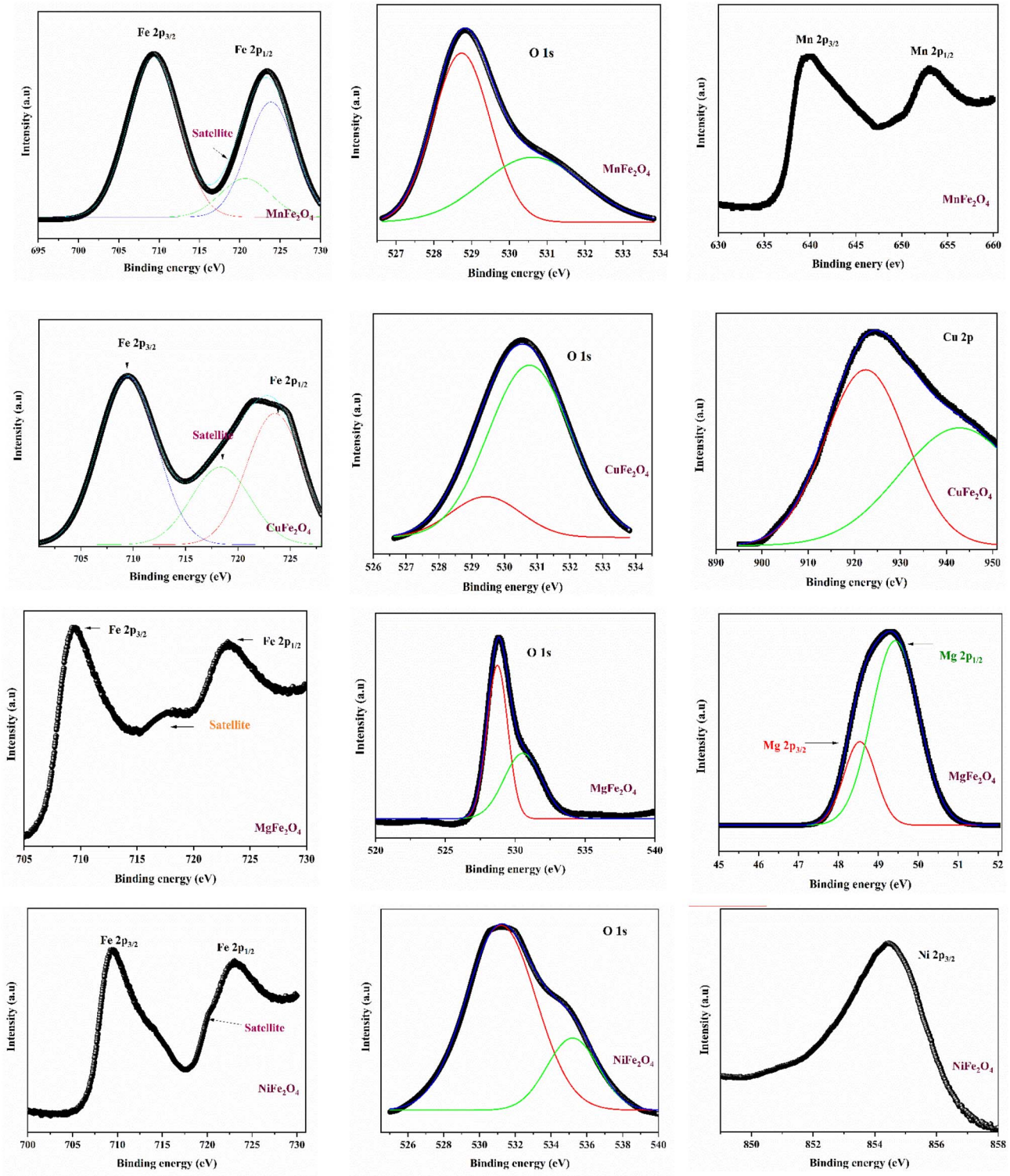

Fig. 7 High resolution X-ray photoelectron spectroscopy (XPS) spectra of the elements of MFe_2O_4 (M^{2+} = Ni, Mg, Cu, Mn) spinel ferrites.

To improve the accuracy of saturation magnetization values, M_s was extrapolated using the law of approach to saturation:[60]

$$M = M_s\left[1 - \frac{a}{H} - \frac{b}{H^2}\right] + kH \quad (4)$$

Fitting the experimental data using eqn (4) allowed the extraction of parameters related to magnetic inhomogeneities (a), magneto-crystalline anisotropy (b), and high-field susceptibility (k). The results show that $CuFe_2O_4$ exhibits higher magnetic inhomogeneity, while $MgFe_2O_4$ and $MnFe_2O_4$ display more homogeneous magnetic behavior.[33]

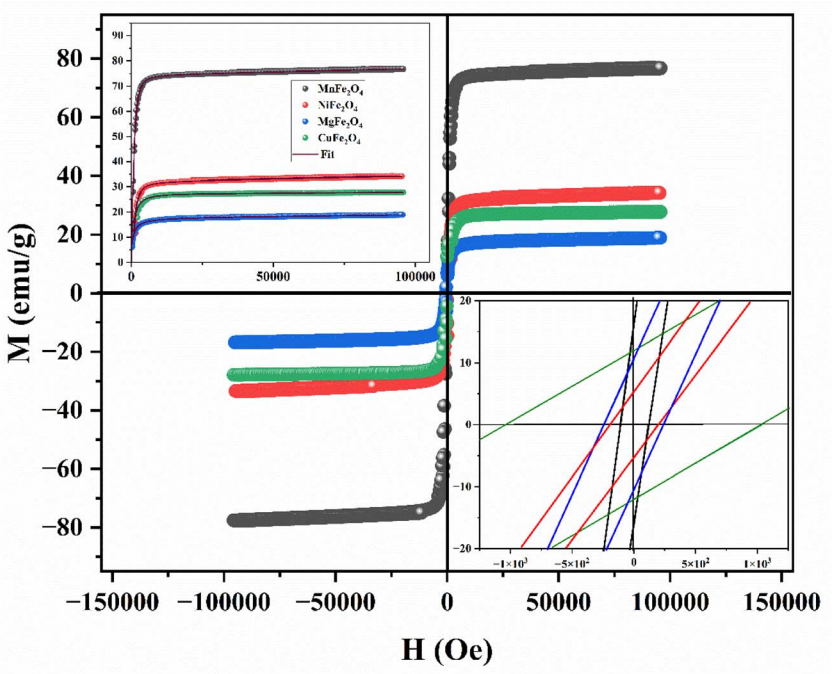

Fig. 8 Magnetic hysteresis loops carried at room temperature MFe_2O_4 (M^{2+} = Ni, Mg, Cu, Mn) spinels ferrites. The top inset shows the fitting of M(H) applying the approach to saturation law (LAS). The bottom inset exhibits the zoom of part of curves near the origin showing remanence (M_r) and coercivity (H_c).

The magnetic moment per formula unit (μ) was calculated using the following relation:[44]

$$\mu = \frac{M \times M_S}{5585} \quad (5)$$

where M_s is expressed in emu per g and M is the molecular weight of the compound. The obtained values follow the order $MnFe_2O_4 > NiFe_2O_4 > CuFe_2O_4 > MgFe_2O_4$, reflecting the nature of the divalent cation and its distribution within the spinel structure. This trend is consistent with Néel's model, where the net magnetic moment arises from the difference between the A and B sublattices:[61]

$$n_{th} = M_B - M_A \quad (6)$$

The calculated magnetic moments show qualitative agreement with experimental results, confirming the dominant role of cation distribution in determining magnetic behavior.[61]

Table 3 Room temperature magnetic parameters of MFe_2O_4 (M = Mn, Cu, Mg, Ni) spinel ferrites carried out at 300 K

Samples	$MnFe_2O_4$	$CuFe_2O_4$	$MgFe_2O_4$	$NiFe_2O_4$
M_s (emu per g)	67.17	22.06	16.69	33.07
M_r (emu per g)	16.65	12.04	45.46	10.44
H_c (Oe)	113.31	1040.60	192.91	240.01
A (Oe)	122.84	182.04	95.12	146.56
b 10^4 (Oe^2)	3.75	6.27	1.21	4.32
k 10^{-6} (emu per g per Oe)	2.96	5.744	1.68	3.06
K_1 10^4 (erg per cm^3)	3.96	12.66	1.51	4.46
μ (μ_B)	2.77	0.95	0.6	1.38
n_{th} (μ_B)	5.00	1.00	0.00	1.99

Finally, the microwave resonance frequency (ω_m) was evaluated using the following relation:[62]

$$\omega_m = 8\pi^2 M_s \gamma \quad (7)$$

where γ (the gyromagnetic ratio) is equal to 2.8 MHz Oe^{-1} and M_s corresponds to the saturation magnetization. The results indicate that the resonance frequency can be tuned by modifying the nature of the divalent cation. This tunability arises

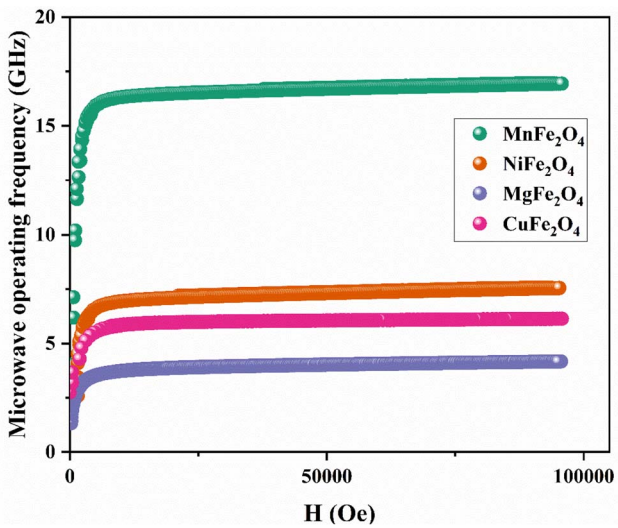

Fig. 9 The evolution of microwave operating frequency *versus* the Applied magnetic field of MFe_2O_4 (M^{2+} = Ni, Mg, Cu, Mn) spinels ferrites.

from the combined influence of saturation magnetization, magneto-crystalline anisotropy, and microstructural parameters, making these materials promising for high-frequency and microwave applications.

3.5 Electrical characterization

3.5.1 Electrical resistivity. Fig. 10 shows the temperature dependence of the electrical resistivity of MFe_2O_4 (M = Mn, Cu, Mg, Ni) spinel ferrites measured in the temperature range 400–700 K. All samples exhibit a decrease in resistivity with increasing temperature, confirming their semiconducting behavior and typical negative Temperature Coefficient of Resistance (NTCR) characteristics.

This behavior is attributed to thermally activated charge transport governed by small polaron hopping between Fe^{2+} and Fe^{3+} ions located at octahedral (B) sites.[63,64] In this mechanism, charge carriers are initially localized and require thermal energy to overcome potential barriers, leading to a decrease in resistivity as temperature increases. The resistivity follows the Arrhenius relation:[63,64]

$$\rho = \rho_0 \exp\left(\frac{E_a}{k_B T}\right) \quad (8)$$

where E_a is the activation energy, k_B is the Boltzmann constant, and ρ_0 is the pre-exponential factor. The activation energies were extracted from the linear fitting of $\ln(\rho)$ *versus* $1/T$ (inset of Fig. 10). The obtained values are 1.25 eV ($MnFe_2O_4$), 1.05 eV ($CuFe_2O_4$), 1.01 eV ($NiFe_2O_4$), and 1.59 eV ($MgFe_2O_4$).

The relatively high activation energy observed for $MgFe_2O_4$ is associated with the non-magnetic nature of Mg^{2+} ions, which reduces the number of available hopping sites and weakens the Fe^{2+}/Fe^{3+} exchange interactions. In contrast, lower E_a values in $MnFe_2O_4$ and $NiFe_2O_4$ indicate more favorable charge transport due to stronger electronic interactions within the spinel lattice.[65]

Fig. 11 presents the temperature coefficient of resistance (TCR) as a function of temperature. The obtained values confirm pronounced NTC behavior, with maximum sensitivities of −4.69%/K ($MnFe_2O_4$), −4.49%/K ($CuFe_2O_4$), −4.73%/K ($NiFe_2O_4$), and −5.31%/K ($MgFe_2O_4$). These values fall within the typical range for high-performance NTC thermistors, demonstrating good thermal sensitivity.[66–68]

The thermistor constant β was determined from the slope of the $\ln(\rho)$ *versus* $1/T$ plots (Fig. 12), according to:[69–71]

$$\rho(T) = \rho_0 \exp\left(\frac{\beta}{T}\right) \quad (9)$$

where β is directly related to the activation energy ($\beta = E_a/k_B$). The consistency between E_a values obtained from Fig. 10 and 12 confirms the reliability of the analysis. The relatively high β values indicate strong temperature dependence of resistivity, which is desirable for thermistor applications.

The stability factor (SF), defined as the ratio between maximum and minimum resistivity values over the studied temperature range, was also evaluated:[69–71]

$$SF = \log\left(\frac{\rho_{max}}{\rho_{min}}\right) \quad (10)$$

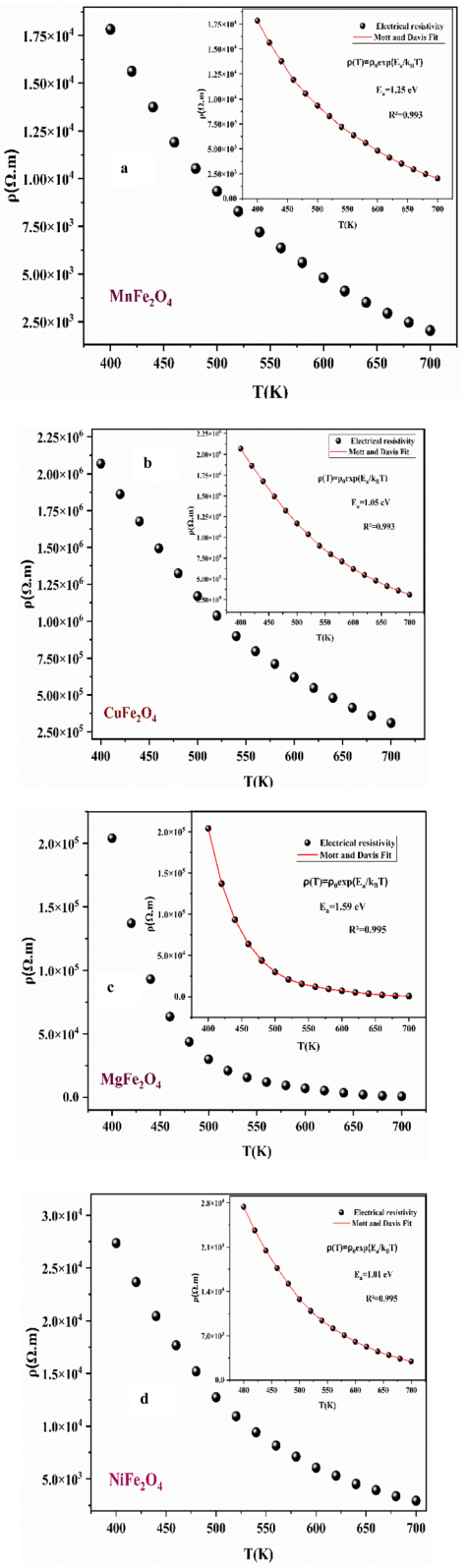

Fig. 10 The evolution of the electrical resistivity *versus* the temperature of MFe_2O_4 spinel ferrites samples: M = Mn (a), Cu (b), Mg (c), and Ni (d), with inset represents the fitted data of the resistivity and the obtained electrical parameters.

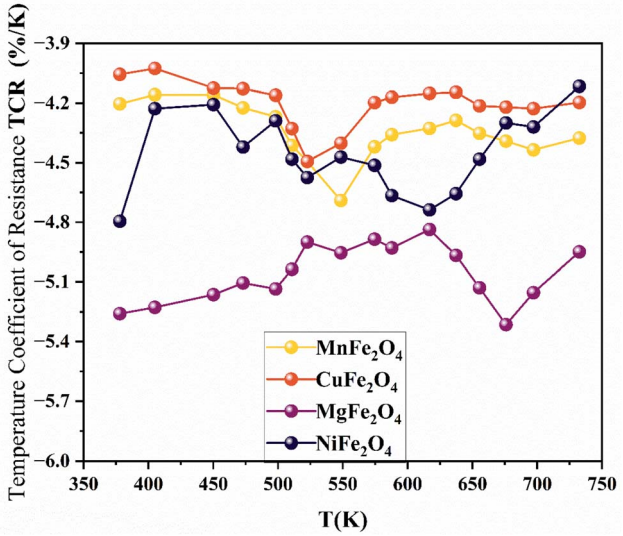

Fig. 11 Variation of the Temperature Coefficient of Resistance (TCR) parameter as a function of the temperature of MFe2O4 (M = Mn, Cu, Mg, Ni) spinel ferrites samples.

The obtained values indicate good thermal stability and reproducibility of the electrical response. In particular, the relatively low SF values observed for $MnFe_2O_4$, $CuFe_2O_4$, and $NiFe_2O_4$ confirm stable resistive behavior, which is essential for reliable sensor performance.[71]

Finally, the temperature sensitivity coefficient (α) was calculated using the standard relation derived from thermistor models:[66,68]

$$\alpha(T) = -\frac{\beta}{T^2} \times 100 \quad (11)$$

The obtained α values range between −4%/K and −5.5%/K, which is consistent with typical NTC thermistor materials. This strong temperature dependence confirms that the studied ferrites are suitable for high-temperature sensing applications.[67,68]

Overall, the electrical properties of MFe_2O_4 ferrites are governed by thermally activated hopping conduction, strongly influenced by cation nature, defect concentration, and cation

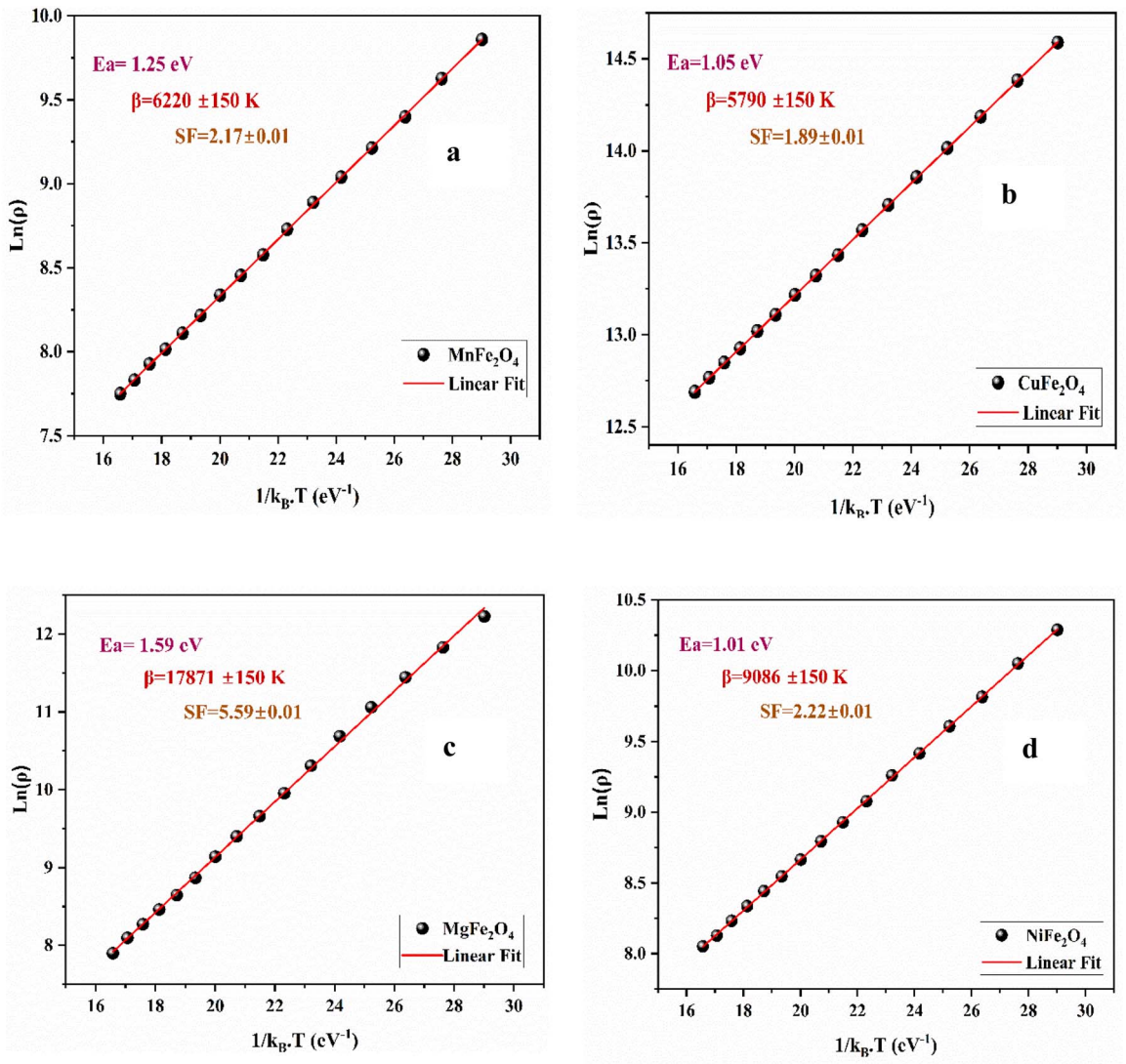

Fig. 12 Evolution of ln (ρ) *vs.* $1/(k_BT)$ of MFe_2O_4 spinel ferrites samples: M = Mn (a), Cu (b), Mg(c), and Ni(d).

distribution within the spinel structure. These results highlight the potential of these materials for thermistor and high-temperature sensing applications.[72–75]

3.6 Outlook and challenges for industrial applications

Despite the promising multifunctional properties of MFe_2O_4 spinel ferrites, several scientific and technological challenges still limit their large-scale industrial deployment. One of the primary issues lies in the precise control of cation distribution between tetrahedral (A) and octahedral (B) sites. This distribution critically governs magnetic anisotropy, electrical conductivity, and dielectric response through A–B superexchange interactions. However, achieving a controlled degree of inversion remains challenging due to thermodynamic equilibrium constraints and kinetic limitations during high-temperature synthesis.[76,77]

Defect engineering represents another key challenge. Intrinsic defects such as oxygen vacancies and cationic disorder strongly influence charge transport through small polaron hopping (Fe^{2+}/Fe^{3+}). While a controlled defect concentration can enhance electrical conductivity and sensing performance, uncontrolled defect formation often leads to instability, aging effects, and poor reproducibility.[77] This remains a major bottleneck for industrial reliability. Advanced approaches such as controlled atmosphere processing, aliovalent doping, and defect compensation strategies are therefore required.[77]

From a processing standpoint, scalability and reproducibility remain critical barriers. Conventional solid-state synthesis typically involves high sintering temperatures, leading to excessive grain growth, microstructural inhomogeneity, and increased energy consumption. These factors not only affect magnetic losses and electrical performance but also hinder compatibility with emerging technologies such as miniaturized and flexible electronic systems.[78]

Another major challenge concerns high-frequency applications. Although spinel ferrites are widely used in microwave devices, achieving an optimal balance between high magnetic permeability and low dielectric/magnetic losses remains difficult, particularly for inverse spinel ferrites such as $NiFe_2O_4$ and $CoFe_2O_4$. This limitation is directly related to intrinsic material parameters (anisotropy, domain wall dynamics) and extrinsic factors (grain size, porosity, defects).[79]

In addition, long-term stability, thermal aging, and environmental robustness are often overlooked but are essential for real industrial applications, especially in high-temperature sensors and thermistors. The lack of standardized protocols for stability evaluation further complicates material qualification. Nevertheless, significant opportunities exist. By tailoring the nature of the divalent cation and optimizing cation distribution, it is possible to engineer ferrites with tunable magnetic softness, enhanced thermal sensitivity, and controlled electrical conductivity. These properties make spinel ferrites strong candidates for next-generation technologies, including high-frequency components, NTC thermistors, gas sensors, and electromagnetic interference (EMI) shielding systems.[80]

Future research should focus on advanced synthesis strategies such as sol–gel, hydrothermal, and thin-film deposition techniques, which offer improved control over microstructure and defect chemistry. Furthermore, integrating experimental approaches with theoretical modeling (*e.g.*, density functional theory) will be essential to better understand cation distribution, defect formation, and structure–property relationships.[80] Such combined approaches can accelerate the rational design and industrial optimization of high-performance spinel ferrite materials.

4 Conclusion

In this work, clear structure–property correlations in MFe_2O_4 (M = Mn, Cu, Mg, Ni) spinel ferrites have been established, highlighting the key role of cation engineering in tuning their multifunctional properties. X-ray diffraction combined with Rietveld refinement confirms the formation of a single-phase cubic spinel structure (space group $Fd\bar{3}m$) for all compositions, with lattice parameters systematically influenced by the ionic radius of the divalent cation (Fig. 13).

XPS analysis confirms the presence of the expected oxidation states (Fe^{3+} and M^{2+}) and provides insight into the surface chemical environment, while Raman spectroscopy further confirms the characteristic vibrational fingerprint of the spinel structure through the observation of five active modes associated with tetrahedral and octahedral sites.

Magnetic measurements reveal a strong dependence of the magnetic properties on the nature of the divalent cation. $MnFe_2O_4$ exhibits the highest saturation magnetization due to the large magnetic moment of Mn^{2+}, whereas $MgFe_2O_4$ shows reduced magnetization because of the non-magnetic character of Mg^{2+}. $NiFe_2O_4$ displays intermediate behavior, while $CuFe_2O_4$ is characterized by enhanced coercivity attributed to Jahn–Teller-induced lattice distortions and increased magnetocrystalline anisotropy. The relatively low coercivity values

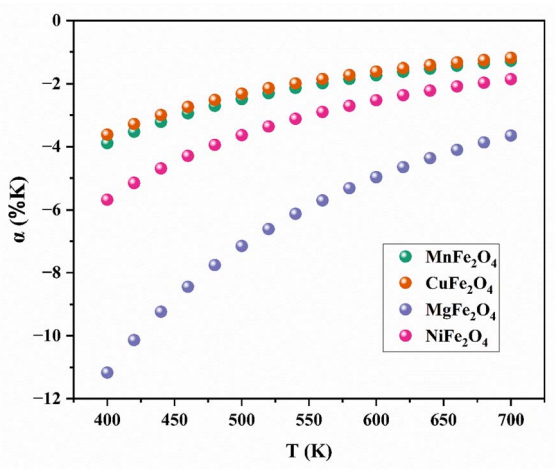

Fig. 13 Temperature dependence of the coefficient α (T) of MFe_2O_4 (M^{2+} = Ni, Mg, Cu, Mn) spinel ferrites.

observed for most samples indicate soft magnetic behavior, suitable for applications requiring low energy losses.

Electrical measurements confirm the semiconducting nature of all compositions, governed by thermally activated hopping conduction. The significant negative temperature coefficient of resistance (NTCR) and high TCR values highlight the strong potential of these materials for thermistor and temperature sensing applications.

Overall, this study demonstrates that the controlled selection of the divalent cation is an effective strategy to tailor the structural, magnetic, and electrical properties of spinel ferrites. These findings provide useful guidelines for the design of high-performance materials for electronic, sensing, and energy-related applications.

Author contributions

Ibtihel Soudani: writing – original draft, visualization, methodology, investigation, formal analysis. Nazir Mustapha: validation, supervision, resources, project administration, methodology. Mokhtar Hjiri: writing – original draft, supervision, methodology.

Conflicts of interest

The authors declare that there is no conflict of interest.

Data availability

The authors confirm that the data used to support the findings of this study are included within the article and are available from the corresponding author upon reasonable request.

Acknowledgements

This work was supported and funded by the Deanship of Scientific Research at Imam Mohammad Ibn Saud Islamic University (IMSIU) (grant number IMSIU-DDRSP2602).

References

1 A. Zaman, A. Ali, H. Shahid, S. H. Alrefaee, S. Knani, V. Tirth and N. Elboughdiri, *RSC Adv.*, 2025, **15**(44), 37050–37061.
2 R. Sharma, S. Bansal and S. Singhal, *RSC Adv.*, 2015, **5**(8), 6006–6018.
3 T. N. Pham, T. Q. Huy and A. T. Le, *RSC Adv.*, 2020, **10**(52), 31622–31661.
4 T. Alammar, M. A. Bedair, N. A. Andreeva, F. Al-Odail, M. A. Alkhalifah, M. E. Owda and A. M. Abuelela, *RSC Adv.*, 2026, **16**(14), 12737–12758.
5 Z. Ali, J. A. Baig, H. I. Afridi, K. Akhtar, S. Perveen and N. Raza, *RSC Adv.*, 2025, **15**(58), 50470–50480.
6 M. M. Hussein, S. A. Saafan, H. F. Abosheiasha, D. Zhou, D. S. Klygach, M. G. Vakhitov and M. A. Darwish, *RSC Adv.*, 2023, **13**(38), 26879–26891.
7 M. D. Hossain, A. T. M. K. Jamil, M. S. Hossain, S. J. Ahmed, H. N. Das, R. Rashid and M. N. I. Khan, *RSC Adv.*, 2022, **12**(8), 4656–4671.
8 J. M. Li, X. L. Zeng and Z. A. Xu, *Appl. Phys. Lett.*, 2013, **103**, 23–30.
9 M. Asif, W. Irshad, M. I. Asif, R. S. Almufarij, Y. M. Alanazi, R. U. Hassan and F. Atamurotov, *J. Mater. Sci.: Mater. Electron.*, 2025, **36**(29), 1–19.
10 T. Prabhakaran and J. Hemalatha, *Ceram. Int.*, 2016, **42**(12), 14113–14120.
11 M. A. Almessiere, A. V. Trukhanov, F. A. Khan, Y. Slimani, N. Tashkandi, V. A. Turchenko and A. Baykal, *Ceram. Int.*, 2020, **46**(6), 7346–7354.
12 N. Mott, *Appl. Phys.*, 1984, **56**, 169–193.
13 A. Manohar, K. Chintagumpala and K. H. Kim, *Ceram. Int.*, 2021, **47**(5), 7052–7061.
14 A. Miller and E. Abrahams, *Phys. Rev.*, 1960, **120**(3), 745–755.
15 M. B. Mohamed and A. M. Wahba, *Ceram. Int.*, 2014, **40**(8), 11773–11780.
16 S. A. Habib, S. A. Saafan, T. M. Meaz, M. A. Darwish, D. Zhou, M. U. Khandaker and M. K. Omar, *Nanomaterials*, 2022, **12**, 931–950.
17 S. K. Kiran and N. Thakur, *Ceram. Int.*, 2022, **48**(4), 4444–4455.
18 Z. Wang, R. Gao, G. Chen, X. Deng, W. Cai and C. Fu, *Ceram. Int.*, 2019, **46**(7), 9154–9160.
19 R. I. Shakirzyanov, A. L. Kozlovskiy, M. V. Zdorovets, A. L. Zheludkevich, D. Shlimas, N. V. Abmiotka and A. V. Trukhanov, *J. Alloys Compd.*, 2023, **954**, 170083.
20 M. M. Salem, L. V. Panina, E. L. Trukhanova, M. A. Darwish, A. T. Morchenko, T. I. Zubar and A. V. Trukhanov, *Compos. Part B Eng.*, 2019, **174**, 107054.
21 Y. Moualhi, H. Rahmouni, M. Gassoumi and K. Khirouni, *Ceram. Int.*, 2020, **46**(15), 24710–24717.
22 R. D. Shannon, *Acta Crystallogr. A*, 1976, **32**(5), 751–767.
23 A. V. Trukhanov, X. Zhao, V. G. Kostishin, D. I. Tishkevich, E. L. Trukhanova, M. A. Almessiere and Z. Sun, *J. Alloys Compd.*, 2024, **986**, 174048.
24 A. V. Trukhanov, M. A. Almessiere, A. Baykal, S. V. Trukhanov, Y. Slimani, D. A. Vinnik and M. Zdorovets, *J. Alloys Compd.*, 2019, **788**, 1193–1202.
25 D. A. Rayan, A. M. Elseman and M. M. Rashad, *Appl. Phys. A*, 2018, **124**(9), 659.
26 C. Iacovita, G. F. Stiufiuc, R. Dudric, N. Vedeanu, R. Tetean, R. I. Stiufiuc and C. M. Lucaciu, *Magnetochemistry*, 2020, **6**, 2–20.
27 S. B. Somvanshi, M. V. Khedkar, P. B. Kharat and K. M. Jadhav, *Ceram. Int.*, 2020, **46**(7), 8640–8650.
28 K. Pubby, K. Vijay Babu and S. Bindra Narang, *Mater. Sci. Eng. B*, 2020, **255**, 114513.
29 U. Holzwarth and N. Gibson, *Nat. Nanotechnol.*, 2011, **6**(9), 534.
30 T. T. N. Nha, P. H. Nam, T. D. Thanh and P. T. Phong, *RSC Adv.*, 2023, **13**(36), 25007–25017.
31 K. H. Maria, S. Choudhury and M. A. Hakim, *Int. Nano Lett.*, 2013, **3**(1), 42.

32 F. Sun, L. Huang, R. Zhang, S. Wang, S. Jiang, Y. Sun and L. J. Geng, *J. Alloys Compd.*, 2020, **834**, 155248.
33 J. Massoudi, M. Smari, K. Nouri, E. Dhahri, K. Khirouni, S. Bertaina and E. K. Hlil, *RSC Adv.*, 2020, **10**(57), 34556–34580.
34 J. P. Singh, R. C. Srivastava, H. M. Agrawal and R. Kumar, *J. Raman Spectrosc.*, 2011, **42**(7), 1510–1517.
35 M. Tan, Y. Köseoğlu, F. Alan and E. Şentürk, *J. Alloys Compd.*, 2011, **509**(39), 9399–9405.
36 P. Chirawatkul, S. Khoonsap, S. Phumying, C. Kaewhan, S. Pinitsoontorn and S. Maensiri, *J. Alloys Compd.*, 2017, **697**, 249–256.
37 S. Aliyeva, S. Babayev and T. Mehdiyev, *J. Raman Spectrosc.*, 2018, **49**(2), 271–278.
38 D. K. Pradhan, S. Kumari, V. S. Puli, P. T. Das, D. K. Pradhan, A. Kumar and R. S. Katiyar, *Phys. Chem. Chem. Phys.*, 2017, **19**(1), 210–218.
39 B. K. Chatterjee, K. Bhattacharjee, A. Dey, C. K. Ghosh and K. K. Chattopadhyay, *Dalton Trans.*, 2014, **43**(21), 7930–7944.
40 K. R. Sanchez-Lievanos, J. L. Stair and K. E. Knowles, *Inorg. Chem.*, 2021, **60**(7), 4291–4305.
41 H. L. Andersen, C. Granados-Miralles, K. M. Ø. Jensen, M. Saura-Múzquiz and M. Christensen, *ACS Nano*, 2024, **18**(14), 9852–9870.
42 S. Wen, B. Chen, J. Zhang, W. Zhan, Z. He and L. Gao, *Crystals*, 2023, **13**, 10–14.
43 N. Nazari, M. M. Golzan and K. Mabhouti, *Sci. Rep.*, 2025, **15**(1), 25169.
44 F. Tiss, S. Hcini, K. Khirouni, E.-K. Hlil and M. Gassoumi, *Ceram. Int.*, 2025, **51**(23), 38979–38989.
45 K. K. Jani, P. Y. Raval, N. H. Vasoya, M. Nehra, M. Singh, N. Jakhar and R. K. Singhal, *Ceram. Int.*, 2022, **48**(21), 31843–31849.
46 B. Yang, Y. Feng, X. Deng, S. Ta, D. Xiong, K. Wen and M. He, *Ceram. Int.*, 2021, **47**(2), 2107–2114.
47 S. V. Nekipelov, O. V. Petrova, A. V. Koroleva, M. G. Krzhizhanovskaya and N. A. Zhuk, *Ceram. Int.*, 2025, **51**(3), 3343–3349.
48 L. Chen, G. Ye, W. Zhou, J. Dijkmans, B. Sels, A. Malfliet and M. Guo, *Ceram. Int.*, 2015, **41**(10), 12651–12657.
49 S. A. Hosseini, A. Niaei, D. Salari, M. C. Alvarez-Galvan and J. L. G. Fierro, *Ceram. Int.*, 2014, **40**(4), 6157–6163.
50 F. A. Al-Agel, E. Al-Arfaj, A. A. Al-Ghamdi, B. D. Stein, Y. Losovyj, L. M. Bronstein and W. E. Mahmoud, *Ceram. Int.*, 2015, **41**(1), 1115–1119.
51 W. Kong, J. Wang, J. Yao and A. Chang, *Ceram. Int.*, 2018, **44**(2), 1455–1460.
52 C. Murugesan, K. Ugendar, L. Okrasa, J. Shen and G. Chandrasekaran, *Ceram. Int.*, 2021, **47**(2), 1672–1685.
53 Z. Peng, X. Fu, H. Ge, Z. Fu, C. Wang, L. Qi and H. Miao, *J. Magn. Magn. Mater.*, 2011, **323**(20), 2513–2518.
54 S. M. Seyedian, A. Ghaffari, A. Mirkhan, G. Ji, S. Tan, S. Ghorbanian-Gezaforodi and R. Peymanfar, *Ceram. Int.*, 2024, **50**(8), 13447–13458.
55 Q. Ni, L. Sun, E. Cao, W. Hao, Y. Zhang and L. Ju, *Ceram. Int.*, 2020, **46**(7), 9722–9728.
56 A. H. Cahyana, A. R. Liandi, Y. Yulizar, Y. Romdoni and T. P. Wendari, *Ceram. Int.*, 2021, **47**(15), 21373–21380.
57 M. A. Wahba, *Ceram. Int.*, 2025, **51**(4), 4329–4342.
58 H. Shokrollahi and K. Janghorban, *J. Mater. Process. Technol.*, 2007, **189**(1), 11–12.
59 M. Kaiser, *Appl. Phys. A*, 2023, **129**(12), 840.
60 F. A. Alfehaid, R. Charguia, S. Hcini, K. Khirouni and M. L. Bouazizi, *Opt. Mater.*, 2024, **154**, 115642.
61 F. Fakhry, E. Shaheen, H. El-Dosoky, T. M. Meaz, M. Mubark and R. El-Shater, *Sci. Rep.*, 2024, **14**(1), 29407.
62 M. L. Bouazizi, S. Hcini, K. Khirouni, M. H. Dhaou, F. Najar and A. H. Alshehri, *J. Electron. Mater.*, 2023, **52**(4), 2878–2893.
63 N. F. Mott, *Philos. Mag.*, 1971, **24**(190), 935–958.
64 N. F. Mott, *J. Non-Cryst. Solids*, 1978, **28**(2), 147–158.
65 N. Ponpandian, P. Balaya and A. Narayanasamy, *J. Phys. Condens. Matter*, 2022, **14**(12), 3221.
66 E. Stefan, P. A. Connor, A. K. Azad and J. T. S. Irvine, *J. Mater. Chem. A*, 2014, **2**, 18106–18114.
67 Y. Moualhi and H. Rahmouni, *Mater. Chem. Phys.*, 2025, **332**, 130185.
68 A. Ghodhbani, Y. Moualhi, W. Dimassi, R. M'nassri, H. Rahmouni and K. Khirouni, *Phys. Rev. B Condens. Matter*, 2024, **683**, 415964.
69 C. Yuan, X. Liu, M. Liang, C. Zhou and H. Wang, *Sens. Actuators, A Phys.*, 2011, **167**(2), 291–296.
70 Z. P. Nenova and T. G. Nenov, *IEEE Trans. Instrum. Meas.*, 2009, **58**(2), 441–449.
71 G. M. Gouda and C. L. Nagendra, *Sens. Actuators, A Phys.*, 2009, **155**(2), 263–271.
72 Y. Q. Gao, Z. M. Huang, Y. Hou, J. Wu, W. Zhou, C. OuYang and J. H. Chu, *Mater. Sci. Eng. B*, 2014, **185**, 74–78.
73 S. Aleksić, N. Obradović, N. S. Mitrović and M. D. Luković, *Sci. Sinter.*, 2024, **56**(3), 299–308.
74 J. E. Kang, J. Ryu, G. Han, J. J. Choi, X. H. Yoon, B. D. Hahn and D. S. J. Park, *J. Alloys Compd.*, 2012, **534**, 70–73.
75 L. Wu, J. Wang, G. Lan, W. Li, P. Meng and S. Jia, *J. Alloys Compd.*, 2025, **1011**, 178396.
76 C. A. Hall, P. Ferrer, D. C. Grinter, S. Kumar, I. da Silva, J. Rubio-Zuazo and R. Grau-Crespo, *J. Mater. Chem. A*, 2024, **12**(43), 29645–29656.
77 M. Baričić, P. Maltoni, G. Barucca, N. Yaacoub, A. Omelyanchik, F. Canepa and D. Peddis, *Phys. Chem. Chem. Phys.*, 2024, **26**(7), 6325–6334.
78 P. Dolcet, S. Diodati, F. Zorzi, P. Voepel, C. Seitz, B. M. Smarsly and S. Gross, Green Chem, *Green Chem.*, 2018, **20**(10), 2257–2268.
79 N. Guijarro, P. Bornoz, M. Prévot, X. Yu, X. Zhu, M. Johnson and K. Sivula, *Sustain. Energy Fuels*, 2018, **2**(1), 103–117.
80 M. D. Hossain, A. T. M. K. Jamil, M. S. Hossain, S. J. Ahmed, H. N. Das, R. Rashid and M. N. I. Khan, *RSC Adv.*, 2022, **12**(8), 4656–4671.